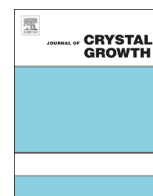




ELSEVIER

Contents lists available at ScienceDirect

Journal of Crystal Growth

journal homepage: www.elsevier.com/locate/jcrysgr

The effect of process parameters on floating zone crystal growth of selected cuprates



Nadja Wizent^{a,b}, Norman Leps^{a,b}, Günter Behr^a, Rüdiger Klingeler^b,
Bernd Büchner^a, Wolfgang Löser^{a,*}

^a Leibniz Institute for Solid State and Materials Research (IFW) Dresden, D-01171 Dresden, Germany

^b Kirchhoff Institute for Physics, Heidelberg University, D-69120 Heidelberg, Germany

ARTICLE INFO

Available online 28 November 2013

Keywords:

A1. Phase equilibria

A2. Floating zone technique

B2. Magnetic materials

B1. Cuprates

ABSTRACT

Process parameters for floating zone crystal growth with optical heating were analyzed with special emphasis to the effect of external gas pressure. The cuprates are grown at low velocities ≤ 1 mm/h and with a traveling solvent floating zone enriched in CuO. Elevated oxygen pressure up to 15 MPa can affect phase equilibria and solidification modes, which enabled crystal growth of various novel compounds, which are not stable at normal pressure. Analyses of quenched zones suggest that crystals grow from oxygen depleted melts. Upon melting at the interface of the feed rod oxygen is released. Undesired formation of gas bubbles in the melt can be partly inhibited by growing under O₂/Ar mixed gas atmosphere. Highly anisotropic antiferromagnetic ordering and strong effects of Ca doping in selected cuprates were revealed on single crystalline samples.

© 2013 Elsevier B.V. All rights reserved.

1. Introduction

Cuprates became unique subjects of physical research after their high- T_c superconducting properties were discovered [1]. Apart from superconductivity some cuprates are excellent model systems for low-dimensional quantum antiferromagnetism [2]. Attempts of floating zone (FZ) crystal growth of cuprates by image furnaces have been previously reviewed by Revcolevschi et al. [3,4]. The traveling solvent floating zone (TSFZ) method is successfully applied because it can supply large single crystals, not contaminated by melt flux or container [5].

Thermodynamic aspects and in particular the role of oxygen pressure are of fundamental interest for both synthesis of cuprates and optimization of their properties [3]. Copper can change its valence from Cu¹⁺ to Cu²⁺. Elevated oxygen pressure even promotes the presence of Cu³⁺ ions in the liquid phase of the binary CuO system, which leads to considerable modification of phase equilibria [6]. The diminished concentration difference between melt and the CuO phase at elevated oxygen partial pressure facilitated higher growth rates [7]. This tight correlation of TSFZ crystal growth parameters and phase diagram features at high oxygen pressure was recently elaborated for the ternary cuprate CoCu₂O₃ [8]. The Cu₃Co₃O phase diagram calculations and experiments revealed that the solidification mode of CoCu₂O₃ changed

from double-peritectic solidification (with respect to metal and oxygen content) at ambient pressure to congruent melting at high oxygen partial pressure. Apart from phase diagram features and ambient atmosphere the outer shape of the floating zone, the melt/crystal interface shape, the velocity and direction of growth, rotation of seed and feed rod, and control of radiation flux in the image furnace are decisive in TSFZ crystal growth of particular cuprates [9].

In the present work process parameters for crystal growth of cuprates by TSFZ methods with optical radiation heating are investigated. One specific aspect is the crystal growth of compounds with extended solid solubility at high oxygen gas pressure in the growth chamber.

2. Experimental details

A ceramic preparation route of feed rods was applied with similar parameters for all materials. In the initial step ingredients, metal oxide or metal carbonate powders, were mixed in stoichiometric proportions. Repeated grinding and sintering steps were carried out and after each sintering process the reaction status was checked by XRD phase analysis. Single phase powder was mandatory for feed rods in most systems. Finally, powders were filled into latex tubes and pressed to rods 6–8 mm in diameter and up to 100 mm in length at hydrostatic pressures up to 40 MPa. The feed rods were sintered at temperatures approximately 900–1000 °C (cf. [10] for details).

* Corresponding author. Tel.: +49 351 4659 647; fax: +49 351 4659 313.
E-mail address: w.loeser@ifw-dresden.de (W. Löser).

Image furnaces with three different designs and optical radiation schemes were applied. The crystal systems Inc. (CSI) image furnace is equipped with four halogen lamps with 300 W power each situated in the focus of an ellipsoidal mirror, arranged in a horizontal plane around the growth chamber [11]. The maximum gas pressure in the growth chamber consisting of a quartz tube is confined to about 1 MPa.

In the vertical double-ellipsoid optical furnace URN-2ZM developed at MPEI Moscow [12] one single xenon lamp with 3 or 5 kW power is located in the focus of the mirror at the bottom. The light is reflected by the two vertically arranged ellipsoid mirrors into the growth chamber situated in the focus of the large second mirror in the upper part of the apparatus. It enables the use of high pressure gas atmospheres up to 8 MPa. The vast majority of growth experiments were conducted with a smart floating zone (SFZ) apparatus designed and constructed at IFW Dresden on the basis of vertical double-ellipsoid furnace scheme [13]. Strong focussing of the light intensity of a xenon lamp up to 7 kW power is controlled by a mechanical light shutter and provides uniform radial heating of the zone. The short growth chamber consisting of a short quartz tube 72 mm in length enables a maximum gas pressure of 15 MPa. For safety reasons at working pressures > 5 MPa a sapphire cylinder with 20 mm wall thickness is applied as container material instead of quartz tubes [10]. The SFZ apparatus is equipped with gas supply for bare gases (Ar, O₂) and Ar/O₂ gas mixtures at high pressure. An in situ temperature measurement by a two-color pyrometer is implemented based on a stroboscopic method [14] (*cf.* also [15]). This method is unique for image furnaces and allows controlling of FZ temperatures and optimizing temperature profiles by changing the lamp position for example [16].

The microstructure and crystal perfection of samples were investigated by optical metallography in polarized light, by scanning electron microscopy (SEM) and by electron probe microanalysis (EPMA) applying the EDX mode. A CuO single crystal was utilized as a standard for the determination of the oxygen content. The oxygen concentration in solid materials was also measured by the carrier gas – hot extraction method (CGHE). For calibration, the composition of samples was verified by chemical analysis using Inductively coupled plasma – optical emission spectrometry (ICP-OES).

The X-ray Laue back-scattering method was utilized to determine the orientation of grown crystals. The magnetic properties have been measured in a MPMS-XL5 SQUID magnetometer.

3. Crystal growth of selected cuprates

3.1. The system $Sr_{14-x}Ca_xCu_{24}O_{41}$

The properties of the $Sr_{14-x}Ca_xCu_{24}O_{41}$ compound, a spin-ladder system with antiferromagnetic behavior, are drastically changed by Ca-doping. For high Ca-doping ($x=13.6$) polycrystalline samples become superconducting under hydrostatic pressure of 3 GPa [17]. Ca-doping is limited under normal pressure, but at elevated oxygen pressure $p_{O_2} \approx 1.3$ MPa single crystals of $Sr_{14-x}Ca_xCu_{24}O_{41}$ up to $x_{Ca}=12$ have been grown by TSFZ [18].

Here, TSFZ growth of $Sr_{14-x}Ca_xCu_{24}O_{41}$ was accomplished under high oxygen pressure $p_{O_2} \leq 15$ MPa with nominal Ca-doping up to $x=13$. In Fig. 1 the grain selection during the initial stage of $Sr_{1.5}Ca_{12.5}Cu_{24}O_{41}$ growth at $p_{O_2}=5$ MPa with velocity $v=0.38$ mm/h is illustrated. The crystal boules exhibits globular coarse grains, where the actual $x_{Ca}=12.4$ determined by EPMA is close to the initial feed rod composition $x_{Ca}=12.5$. Higher growth velocity, $v=1$ mm/h, resulted in reduced Ca-doping $x_{Ca}=12.2$ and columnar grain structure. The observation is adverse to the prediction of the Burton–Prime–Slichter theory [19] where

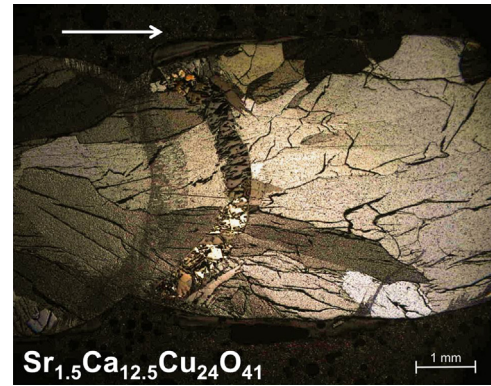


Fig. 1. Optical image in polarized light (longitudinal section) showing grain selection in initial state of $Sr_{1.5}Ca_{12.5}Cu_{24}O_{41}$ crystal growth at 5 MPa oxygen high pressure with $v=0.38$ mm/h. The arrow indicates the growth direction.

distribution coefficients approach unity with increasing growth velocity. We therefore attribute the effect to sluggish interface attachment kinetics of Ca-ions.

In both cases during the initial state instabilities for characteristic peritectic growth in form of periodic bands of Ca-rich phases (Ca_2CuO_3) occurred. To some extent the growth instabilities are caused by non-homogeneous melting of the feed rod under non-optimized radiation conditions. In semi-solid areas of the partially molten rod surface Ca-rich refractory phases can be formed. If grains break off from the feed rod accidentally, they cause mechanical instabilities and composition fluctuations in the floating zone.

Therefore, light flux conditions were optimized by a ‘light blocker’. A circular diaphragm was placed at the optical axis above the common focus of the two vertically arranged mirrors. According to the principles of irradiation profile formation of the vertical double-ellipsoid optical configuration considered in Ref. [16] it reflects light beams nearly parallel to the optical axis. After reflection at the upper mirror these grazing light rays can lead to undesired partial melting at the feed rod surface. Using the ‘light blocker’ light beams with high-incidence angle at the irradiated zone promote a sharp interface and apparently stabilize the growth process. Moreover, mixing of the melt was forced by counter-rotation of feed rod and crystal with typical rotation rates of 5–15 rpm and 10–30 rpm, respectively.

The analysis of the quenched floating zone showed that the melt is Cu- and Sr-rich but Ca-depleted. The oxygen content is 3–4 at% lower than that of the crystal, which was reproduced for growth experiments with different Ca contents x . Therefore, we suppose that crystals grow from oxygen depleted melts.

An upper limit of Ca doping, $x_{Ca}=12.7$, in crystal boules with coarse grains ($\varnothing \sim 2\text{--}4$ mm) was achieved for the feed rod composition $Sr_1Ca_{13}Cu_{24}O_{41}$ under $p_{O_2}=15$ MPa, the highest pressure applied. This resembles the reported crystal growth of $Sr_1Ca_{13}Cu_{24}O_{41}$ at elevated pressure $p_{O_2}=3.5$ MPa and $v=0.7$ mm/h [20]. The growth of $Ca_{14}Cu_{24}O_{41}$ failed even at highest values of $p_{O_2}=5$ MPa and $v=1$ mm/h. Instead, striation-like crystallization was observed of Ca_2CuO_3 and a compound with the formal stoichiometry $CaCu_3O_4$. According to X-ray analyses the latter phase exhibits $CaCu_2O_3$ tetragonal (Pmmn) structure, but Ca lattice sites are partially occupied by Cu, leading to a composition $Ca_{0.75}Cu_{0.25}Cu_2O_3$ and lattice constants $a=0.9823$ nm, $b=0.4054$ nm $c=0.3430$ nm at $p_{O_2}=5$ MPa [10]. The unit cell volume is smaller than that of $CaCu_2O_3$ crystals grown at normal pressure.

3.2. The system $Ca_{2+x}Y_{2-x}Cu_5O_{10}$

The compounds $Ca_{2+x}Y_{2-x}Cu_5O_{10}$ belong to a one-dimensional spin chain system where the formal copper valence depends on Ca

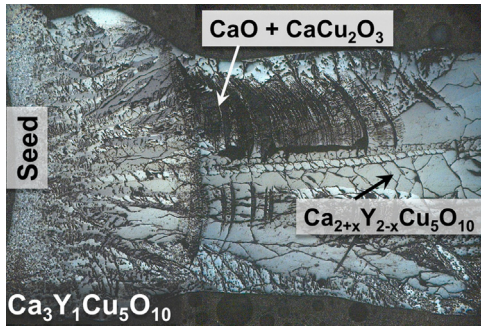


Fig. 2. Optical image in polarized light (longitudinal section) showing initial part of $\text{Ca}_3\text{Y}_1\text{Cu}_5\text{O}_{10}$ crystal growth at 0.98 MPa oxygen pressure with $v=0.38$ mm/h.

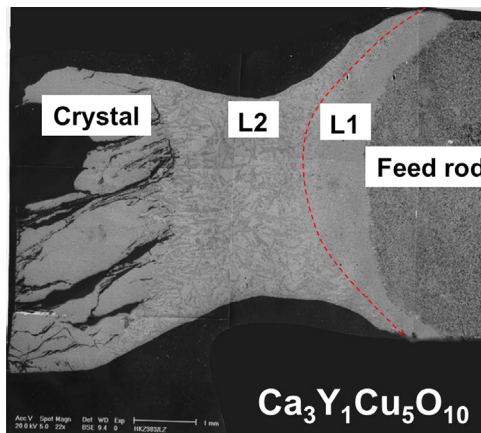


Fig. 3. SEM image of the quenched zone located between $\text{Ca}_3\text{Y}_1\text{Cu}_5\text{O}_{10}$ crystal and feed rod. Liquid phase separation between the Y-rich melt L_1 near the feed rod and Y-depleted melt L_2 near the crystal is indicated.

doping. At 1000 °C in air they melt incongruently and exhibit a single-phase solid solution range of Ca, $0 \leq x \leq 0.8$ [21]. Crystals where previously grown by TSFZ under elevated oxygen pressure up to 1 MPa for a wide range of Ca doping $0 \leq x \leq 1.67$ [22]. We have grown the undoped compound $\text{Ca}_2\text{Y}_2\text{Cu}_5\text{O}_{10}$ under normal pressure 0.1 MPa, but Ca-rich crystals $\text{Ca}_{2+x}\text{Y}_{2-x}\text{Cu}_5\text{O}_{10}$ up to $x=1.88$ at $p_{\text{O}_2}=6$ MPa from feed rods with $x \leq 1.9$. Crystal growth is challenging and crystals with high Ca contents are hygroscopic and difficult to handle because they are prone to cracking during preparation of specimen. Crystal growth of $\text{Ca}_3\text{Y}_1\text{Cu}_5\text{O}_{10}$ at $p_{\text{O}_2}=9.8$ MPa is illustrated in Fig. 2. At the start grain selection from a polycrystalline seed with the same composition as the feed rod occurs simultaneously with the crystallization of narrow bands of secondary phases, CaO containing insignificant fractions of CaCu_2O_3 . The steady state growth of single phase $\text{Ca}_{2+x}\text{Y}_{2-x}\text{Cu}_5\text{O}_{10}$ is reached after about 10–15 mm.

The overall composition of the quenched final zone after TSFZ growth of $\text{Ca}_{2+x}\text{Y}_{2-x}\text{Cu}_5\text{O}_{10}$ is CuO-rich similar to other cuprates as proved by EPMA. As representative example the zone quenched after crystal growth of $\text{Ca}_3\text{Y}_1\text{Cu}_5\text{O}_{10}$ is shown in Fig. 3. From the microstructure a significant composition gradient is apparent caused by solidification fronts moving from the solid/melt interfaces toward the center along the zone axis. Moreover, we have revealed a sharp boundary in the quenched zone between an about one millimeter thick Y-rich layer adjacent to the feed rod, which can be distinguished from the Y-lean residual part. The distinct boundary suggests possible liquid phase separation in the FZ between Y-rich and Y-lean melts L_1 and L_2 , respectively, as indicated in Fig. 3. This unique behavior was not detected in any other cuprate system.

3.3. The system $\text{Ca}_{2+x}\text{Nd}_{2-x}\text{Cu}_5\text{O}_{10}$

The $\text{Ca}_{2+x}\text{Nd}_{2-x}\text{Cu}_5\text{O}_{10}$ cuprates are one more one-dimensional spin chain system, where Y is substituted by Nd another trivalent ion with larger diameter. Compared to the isostructural $\text{Ca}_{2+x}\text{Y}_{2-x}\text{Cu}_5\text{O}_{10}$ it exhibits a narrower single-phase solid solution range for Ca at 1000 °C in air, approximately $0 \leq x \leq 0.3$ [21]. So far no attempts of crystal growth are known from literature.

The image of a $\text{Ca}_2\text{Nd}_2\text{Cu}_5\text{O}_{10}$ crystal is shown in Fig. 4 along with characteristic sections. It was grown from a stoichiometric feed rod at $v=0.5$ mm/h in O_2/Ar mixed gas atmosphere at 0.1 MPa. From the beginning a traveling solvent with CuO excess was used in form of a disk 5 mm in length. This considerably reduced the time to reach the steady state and accelerated the grain selection as illustrated in the longitudinal section Fig. 4b. In the initial part bands of $(\text{Ca,Nd})_{14}\text{Cu}_{24}\text{O}_{41}$ and small particles of Nd_2CuO_4 are distributed between the $\text{Ca}_2\text{Nd}_2\text{Cu}_5\text{O}_{10}$ columnar grains, which expand in dimensions until one grain covers the whole cross-section (Fig. 4c). The facets at the surface point to the single crystalline nature of the rod (Fig. 4a), however, the crystal suffers from cracks caused by thermal stresses on cooling. The quenched last zone exhibits inhomogeneous microstructure (Fig. 4d). Dendrites of the $\text{Ca}_2\text{Nd}_2\text{Cu}_5\text{O}_{10}$ primary phase solidify along with interdendritic CuO particles and small eutectic fractions, which could not be identified unambiguously. The average solvent composition of the quenched zone was determined by EPMA with about ± 1 at% accuracy of the mapping. The solvent composition 7.7 at% Ca 7.8 at% Nd 38.4 at% Cu 46.1 at% O differs considerably from the crystal, 10.5 at% Ca 10.5 at% Nd 26.3 at% Cu 52.7 at% O, not only by ≈ 12 at% excess Cu, on expense of Ca and Nd, but also by ≈ 6 at% O_2 deficiency. This analysis of the as-solidified FZ suggests that the crystal has been grown from an oxygen-depleted solvent. Though, there is an uncertainty about oxygen loss during the re-solidification process despite the fast quenching. Conversely, on melting the feed rod excess oxygen is released at the interface. This can lead to the formation of undesired gas bubbles in the melt if its oxygen solubility limit is exceeded. Using an Ar/O_2 gas mixture (instead of pure oxygen) the reduced oxygen partial pressure p_{O_2} in the ambient atmosphere stimulated the diffusional exchange with the molten zone and effectively inhibited bubble formation. Gas bubbles, which can also originate from the porous ceramic feed rods, destabilize the FZ growth process and reduce the crystal perfection.

For higher Ca doping ($x > 0$) crystals have been grown only at elevated oxygen gas pressure. A $\text{Ca}_{2.5}\text{Nd}_{1.5}\text{Cu}_5\text{O}_{10}$ crystal was achieved with $v=0.4$ mm/h at $p_{\text{O}_2}=4$ MPa. In the initial part alternating layers of $\text{Ca}_{2+x}\text{Nd}_{2-x}\text{Cu}_5\text{O}_{10}$ and $(\text{Ca,Nd})\text{Cu}_2\text{O}_3$ phases crystallize before the steady growth is reached. The Ca doping of the crystal $x=0.3$ – 0.4 is somewhat reduced with respect to the nominal feed rod composition ($x=0.5$). Moreover, we detected periodic CaO precipitates in the crystal matrix caused by melting instabilities of the feed rod. In the final cross section the single crystal is partially surrounded by a polycrystalline rim. This requires further optimization of the radiation profile and/or faster seed rotation to flatten the convex crystal/melt interface. No regular crystal growth was realized for high Ca doping in $\text{Ca}_3\text{Nd}_1\text{Cu}_5\text{O}_{10}$. The grain selection failed and only some columnar grains, ~ 1 mm in diameter, were attained with fluctuating Ca content, approaching $x=0.8$ – 0.9 in the final part.

4. Magnetic properties of selected cuprates

Structure and magnetic properties of various single crystalline samples have been extensively studied [10]. Here we can only refer to certain measurements, which illustrate basic features of the

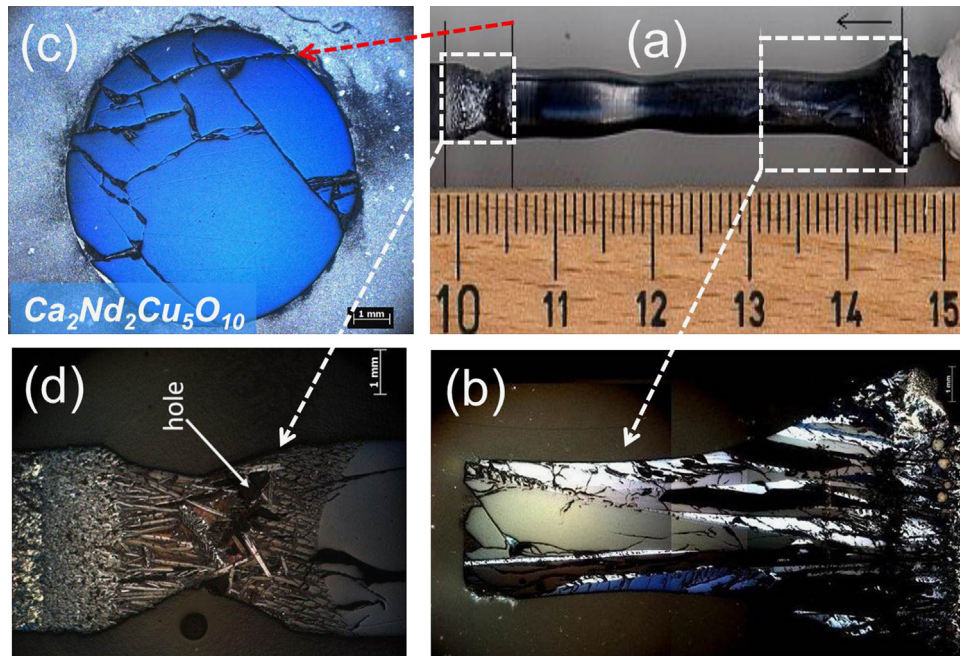


Fig. 4. (a) $\text{Ca}_2\text{Nd}_2\text{Cu}_5\text{O}_{10}$ crystal boule, grown at elevated oxygen high pressure 4 MPa and $\nu=2$ mm/h. The growth direction is indicated by an arrow. The occurrence of outer facets signaling the single crystal is designated by a white vertical line. (b) Optical image in polarized light of the initial part illustrating grain selection from a polycrystalline seed. (c) Cross section of the $\text{Ca}_2\text{Nd}_2\text{Cu}_5\text{O}_{10}$ crystal. (d) Quenched last zone between feed rod (left) and crystal (right). Shrinking holes in the central part are highlighted by an arrow.

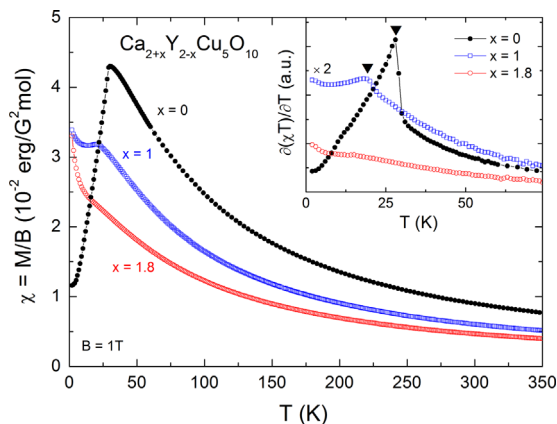


Fig. 5. Static magnetic susceptibility $\chi=M/B$ of $\text{Ca}_{2+x}\text{Y}_{2-x}\text{Cu}_5\text{O}_{10}$ single crystalline samples vs. temperature showing the effect of Ca doping ($x=0, 1, 1.8$) on the long ranged antiferromagnetically ordered phase. Inset: Magnetic specific heat as calculated from the static susceptibility $\chi(T)$. Data for $x=1$ are enlarged by a factor of 2. Black triangles mark the onset of long-range antiferromagnetic order.

grown materials. The temperature dependant static magnetic susceptibility $\chi=M/B$ of a $\text{Ca}_{2+x}\text{Y}_{2-x}\text{Cu}_5\text{O}_{10}$ single crystal is shown in Fig. 5. For $x=0$ and 1, the data imply long range antiferromagnetic order at low temperature. For $x=0$, the data show a pronounced magnetic anisotropy with the easy magnetic axis being $\parallel b$ -axis. Analyzing the magnetic specific heat which is proportional to $\partial(\chi T)/\partial T$ (see inset to Fig. 5) shows that the onset of long-range magnetic order is associated with a pronounced lambda-like anomaly. In addition, pronounced magnetic entropy changes are observed well above the magnetic ordering temperature. Qualitatively, this is in agreement with strong frustration in the spin chains of $\text{Ca}_2\text{Y}_2\text{Cu}_5\text{O}_{10}$ which has been established recently. It has been found that in-chain nearest neighbor exchange $J_1 = -170$ K and next-nearest neighbor coupling $J_2 = 32$ K yield a frustration $|J_2/J_1| \sim 0.19$ [23]. The material is hence at the ferromagnetic side of the phase diagram and very close to the critical

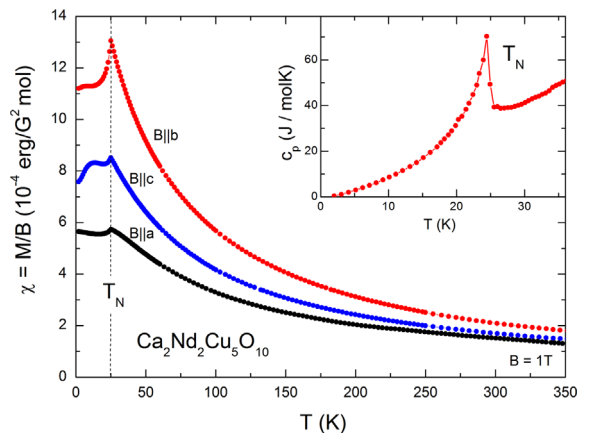


Fig. 6. Static magnetic susceptibility $\chi=M/B$ vs. temperature of a $\text{Ca}_2\text{Nd}_2\text{Cu}_5\text{O}_{10}$ single crystal at $B=1\text{T}$ directed parallel to a -, b -, and c -axis, respectively. The Néel temperature T_N is marked by the dashed line. Inset: Specific heat of $\text{Ca}_2\text{Nd}_2\text{Cu}_5\text{O}_{10}$.

point. Upon increasing the Ca content, the Néel temperature decreases from $T_N=28$ K ($x=0$) to $T_N=18$ K ($x=1$) similarly as observed in Ref. [22], and the associated specific heat anomaly shrinks accordingly. At higher Ca doping, $x=1.8$, there is no indication of antiferromagnetic long range order.

Both long range magnetic order and pronounced magnetic anisotropy at high temperatures is demonstrated for single crystals of undoped $\text{Ca}_2\text{Nd}_2\text{Cu}_5\text{O}_{10}$ in Fig. 6. The magnetic susceptibility discloses antiferromagnetic long range order below $T_N=24$ K. The anomaly of $\chi(T)$ is perceptible for magnetic fields (1T) directed parallel to magnetic easy axis, the b -axis of the monoclinic unit cell, whereas for the other two directions only minute cusps are observed. For comparison the specific heat capacity measurements are shown (inset to Fig. 6), which exhibit a λ -type singularity at the same temperature T_N . Ca doping diminished the ordering temperature to $T_N=17$ K in $\text{Ca}_3\text{Nd}_1\text{Cu}_5\text{O}_{10}$ crystals.

5. Summary and conclusions

Based on numerous TSFZ experiments key process parameters for crystal growth of selected cuprates were analyzed with special emphasis to the effect of elevated gas pressure. High oxygen partial pressure up to 15 MPa in the growth chamber of the mirror furnace can affect the thermodynamic equilibria and enabled the growth of novel cuprates with high Ca doping not stable at normal pressure. Incongruent melting of the compounds causes considerable composition differences at the crystal/melt interface and requires small growth velocities, typically ≤ 1 mm/h, and counter-rotation of crystal and feed rod for convective mixing of constituents in the floating zone. Optimized light flux with strong focussing of radiation for steep temperature gradients and elimination of grazing rays from the incident light flux by a light blocker is favorable for a stable growth process. By using O₂/Ar gas mixtures the oxygen partial pressure in the growth chamber is controlled independently and undesired gas bubble formation in the floating zone is diminished. Magnetic and thermodynamic measurements on single crystalline samples reveal highly anisotropic magnetic properties, pronounced anomalies associated with the onset of long range antiferromagnetic ordering, and a strong effect of Ca doping on the Néel temperatures of the cuprates investigated.

Acknowledgment

The authors thank S. Pichl and S. Müller-Litvanyi for experimental and technical assistance and Dr. W. Gruner and Dr. H. Ehrenberg for chemical analyses. Support by Deutsche Forschungsgemeinschaft via projects BE1749/8 and KL1824/5, and by BMBF within Project 03SF0397 is gratefully acknowledged.

References

- [1] J.G. Bednorz, K.A. Müller, *Z. Physik* 64 (1986) 189–193.
- [2] H.-J. Mikeska, A. Kolezhuk, *One-Dimensional Magnetism*, in: U. Schollwöck, J. Richter, D.J.J. Farnell, et al., (Eds.), *Lecture Notes in Physics 645: Quantum Magnetism*, Springer, Berlin, ISBN 3-540-21422-42004, pp. 1–83 (ISSN 0075-8450).
- [3] A. Revcolevschi, J. Jegoudez, *Prog. Mater. Sci.* 42 (1997) 321–339.
- [4] A. Revcolevschi, A. Vietkine, H. Moudden, *Physica C* 282–287 (1997) 493–494.
- [5] S. Takekawa, H. Nozaki, A. Umezono, K. Kosuda, M. Kobayashi, *J. Cryst. Growth* 92 (1988) 687–690.
- [6] L. Schramm, G. Behr, W. Löser, K. Wetzig, *J. Phase Equilib. Diff.* 26 (2005) 605–612.
- [7] G. Behr, W. Löser, M.-O. Apostu, W. Gruner, M. Hücker, L. Schramm, D. Souptel, J. Werner, *Cryst. Res. Technol.* 40 (2005) 21–25.
- [8] N. Wizent, L. Schramm, G. Behr, W. Löser, W. Gruner, A. Voß, B. Büchner, L. Schultz, *J. Solid State Chem.* 182 (2009) 2036–2040.
- [9] G. Behr, W. Löser, N. Wizent, P. Ribeiro, M.-O. Apostu, D. Souptel, *J. Mater. Sci.* 45 (2010) 2223–2227.
- [10] N. Wizent, PhD Thesis, TU Dresden, 2009 (<http://d-nb.info/1007715715/34>).
- [11] S.M. Koohpayeh, D. Fort, A. Bradshaw, J.S. Abell, *J. Cryst. Growth* 311 (2009) 2513–2518.
- [12] A.M. Balbashov, S.K. Egorov, *J. Cryst. Growth* 52 (1981) 498–504.
- [13] G. Behr, W. Löser, D. Souptel, G. Fuchs, I. Mazilu, C. Cao, A. Köhler, L. Schultz, B. Büchner, *J. Cryst. Growth* 310 (2008) 2268–2276.
- [14] G. Behr et al., German Patent DE 10 2006 019 807.7 (21.04.2006) and PCT/EP2007/05157 (07.03.2007).
- [15] (<http://www.scidre.de/>).
- [16] D. Souptel, W. Löser, G. Behr, *J. Cryst. Growth* 300 (2007) 538–550.
- [17] M. Uehara, T. Nagata, J. Akimitsu, H. Takahashi, N. Mori, K. Kinoshita, *J. Phys. Soc. Jpn.* 65 (1996) 2764–2767.
- [18] U. Ammerahl, G. Dhalenne, A. Revcolevschi, J. Berthon, H. Moudden, *J. Cryst. Growth* 193 (1998) 55–60.
- [19] J.A. Burton, R.C. Prim, W.P. Slichter, *J. Chem. Phys.* 21 (1953) 1987–1991.
- [20] G. Deng, D.M. Radheep, R. Thiyagarajan, E. Pomjakushina, S. Wang, N. Nikseresht, S. Arumugam, K. Conder, *J. Cryst. Growth* 327 (2011) 182–188.
- [21] P.K. Davies, E. Caignol, T. King, *J. Am. Ceram. Soc.* 74 (1991) 569–573.
- [22] K. Kudo, S. Kurogi, Y. Koike, T. Nishizaki, N. Kobayashi, *Phys. Rev. B* 71 (2005) 104413.
- [23] R.O. Kuzian, et al., *Phys. Rev. Lett.* 109 (2012) 117207.